

Kinematics and Structure of Ionized Gas in the UCHII Regions of W33 Main

DAN BEILIS,¹ SARA BECK,¹ AND JOHN LACY²

¹*Raymond and Beverly Sackler School of Physics and Astronomy
Tel Aviv University
Tel Aviv, 69978, Israel*
²*Department of Astronomy
University of Texas
Austin, TX 78712, USA*

(Received August 3, 2021; Accepted MNRAS January 22, 2022)

ABSTRACT

High mass proto-stars create Ultra-Compact H II regions (UCHII) at the stage of evolution when most of the accretion is finished but the star is still heavily embedded in molecular material. The morphologies of UCHII regions reflect the interactions of stellar winds, stellar motions, and density structure in the molecular cloud; they are complex and it has been very difficult to interpret them. We here present data obtained with TEXES on the NASA IRTF of the [NeII] emission line in the proto-cluster of young OB stars in W33 Main. The data cube has a spatial resolution of ~ 1.4 arcsec and true velocity resolution ~ 5 km s⁻¹; with $A_\lambda \sim 0.02A_V$ it is relatively unaffected by extinction. We have run 3D hydrodynamic and line profile simulations, using PLUTO and RADMC-3D, of the gas structures created by multiple windy stars moving relative to each other through the ambient cloud. By iterative comparison of the data cube and the simulations, we arrive at models that reproduce the different morphology and kinematic structure of each UCHII region in W33 Main. The results indicate that each sub-source probably holds multiple exciting stars, permitting an improved view of the stellar population, and finds the stellar trajectories, which may determine the dynamical development of the proto-cluster.

Keywords: ISM: H II Regions, ISM: Kinetics and Dynamics, Stars: Formation, Methods: Numerical

1. INTRODUCTION

Young Stellar Objects (YSOs) of $M_* \gtrsim 8M_\odot$ evolve very fast and can become strong sources of heat, luminosity and ionization while still deeply embedded in the natal molecular cloud. They cannot be seen at optical, UV or the shorter IR wavelengths because of the high extinction. They are most readily observed via the Ultra-Compact H II Regions (UCHII) they excite. UCHII regions are defined by Wood & Churchwell (1989a), to have diameters ≤ 0.1 pc, emission measures $\geq 10^7$ pc cm⁻⁶ and electron densities $\geq 10^4$ cm⁻³. Stars spend on order $\sim 10^5$ yr, much longer than the free expansion time, in this stage: thus presenting the 'lifetime problem' in UCHII regions. This is a crucial stage in star formation as UCHII regions can have significant effects on the surrounding clouds.

Radio continuum observations of UCHII regions find complex morphologies, classified by Wood & Churchwell (1989a) as spherical, cometary, irregular, core-halo and shell ((Kurtz, Churchwell, & Wood 1994); Walsh et al. (1998)). It is not usually possible to deduce how a given UCHII region has evolved and will develop from its appearance alone; to disentangle all the possible mechanisms needs kinematic data as well. Data on the gas kinematics in UCHII regions is however very limited. Optical tracers cannot be used because of the high extinction. Radio recombination lines of H I are observable, but are limited in velocity resolution: thermal broadening of H I in a 10^4 K H II region is $\simeq 20$ km s⁻¹, within a factor of 2 of the typical FWHM observed. The mid-infrared fine structure emission lines of common metals

have proven to be useful kinematic tracers in obscured H II regions. They have the advantage over H I recombination lines that they are broadened less by thermal motions, and they are much less affected by extinction than any optical emission lines. (Zhu et al. 2008; Jaffe et al. 2003) used the $12.8\ \mu\text{m}$ line of [NeII] to probe the internal gas motions in some UCHII regions and Beck et al. (2015, 2020) used [NeII] $12.8\ \mu\text{m}$ and [SIV] $10.5\ \mu\text{m}$ to study gas motions in embedded extragalactic super star clusters. This paper presents high resolution observations of the UCHII regions in the Galactic star-forming region W33-Main in the form of a full 3-D cube of the [NeII] line with ~ 1.4 arcsec spatial and $\sim 5\ \text{km s}^{-1}$ velocity resolution.

Many mechanisms including star-cloud interactions, structures in the ambient cloud, stellar winds and stellar motions can affect the appearance and kinematics of the UCHII region. In this paper we focus on the effects of ionizing, windy stars moving through the cloud. We use PLUTO and RADMC-3D to produce a suite of 3-D hydrodynamic simulations and simulated line profiles of moving stars, which we interactively tweak to create models of each UCHII region in W33 that reproduce the observed spatial and kinematic structures in the data cube. We review W33 and the observations in the next section, the numerical simulation methods in Section 3, and the results in Section 4. In Sections 5 we discuss the implication of our findings for the embedded stellar population and in Section 6 the potential value of this method. These simulations show the effects of multiplicity in each source and the trajectories of the included stars and suggest the future evolution of the proto-cluster.

2. TARGET AND OBSERVATIONS

2.1. W33 Main

W33 is a giant molecular cloud complex in the Galaxy’s Scutum spiral arm (Immer et al. 2013) at a distance ~ 2.4 kpc; $1\ \text{arcsec} \sim 0.12\ \text{pc}$ on the source. In it lies a $\sim 10\ \text{pc}$ star formation region including all evolutionary stages from inactive clumps to fully developed H II regions (Immer et al. 2014). W33 Main is the central molecular clump in the W33 complex. It has molecular mass of $\sim 3965\ M_{\odot}$ (Immer et al. 2014) and multiple signs of active massive star formation, including water and methanol masers (Genzel & Downes 1977; Haschick, Menten, & Baan 1990). The molecular gas in W33 has two velocity components at $+35$ and $+58\ \text{km s}^{-1}$ (Kohno et al. 2018) and these two velocities are seen also in the H134 α recombination line measured over the full 10 arcmin extent of the clouds (Gardner, Wilson, & Thomasson 1975). It holds a small cluster of embedded H II regions detected in the infrared at $3.4\text{--}33\ \mu\text{m}$ by Dyck & Simon (1977) and in the radio by Haschick & Ho (1983). The radio measurements suggest that the exciting stars are a ZAMS cluster of spectral types between O7.5 and B1.5. From maps of the infrared fine-structure lines of [NeII] $12.8\ \mu\text{m}$ and [Ar III] $8.99\ \mu\text{m}$ Beck, Kelly, & Lacy (1998) estimate the spectral types to be O6–O7 and that each sub-source probably contains one exciting star. We will suggest in this paper that the reality may be much more complicated.

2.2. Observations

A data cube of the [NeII] $12.8\ \mu\text{m}$ ($780.42\ \text{cm}^{-1}$) line was obtained at the NASA Infrared Telescope Facility (IRTF) on the night of 2009 July 13 with the University of Texas echelle spectrograph TEXES (Lacy et al. 2002). TEXES is a high resolution spectrograph for wavelengths $5\text{--}25\ \mu\text{m}$ based on a 256×256 element Raytheon Si:As array. The diffraction and seeing limited beam size on the IRTF is $1.4\ \text{arcsec}$ and the spectral resolution, including thermal and instrumental effects, is $\sim 4\ \text{km s}^{-1}$. Each pixel along the N-S oriented slit was $0.36\ \text{arcsec}$; the slit was $1.37\ \text{arcsec}$ wide and $9.3\ \text{arcsec}$ long. The telescope was stepped $0.7\ \text{arcsec}$ east-west across the source and subsequent scans separated by $5\ \text{arcsec}$ in declination; the ends of the scan were used for sky subtraction and the overlap to check and correct the matching of scan positions. No scans had to be shifted more than $2\ \text{arcsec}$ to match the next scan; pointing errors were $< 1\ \text{arcsec}$. The scans were interpolated to create data cubes with pixels $0.6\ \text{arcsec} \times 0.6\ \text{arcsec} \times 0.92\ \text{km s}^{-1}$ and $0.36\ \text{arcsec} \times 0.36\ \text{arcsec} \times 0.92\ \text{km s}^{-1}$. Both cubes are available online and the links given in the Appendix. This paper is based on the first cube, which samples each beam width twice.

Atmospheric lines were used for wavelength calibration and a laboratory blackbody for flux calibration. We estimate the accuracy of the velocity registration to be $\pm 1\ \text{km s}^{-1}$. The spatial position was registered by comparison to the radio interferometer maps and is estimated to be accurate to $\pm 2\ \text{arcsec}$. The data cube’s 0th and 1st moment maps along the spectral axis are shown in Figure 1, and Figure 2 shows the 0th moment maps along the two spatial axes, displaying the velocity extent of the emission in each source.

Figures 1 and 2 show clearly that the ionized gas is concentrated into at least three UCHII regions distinct in space and velocity. Within each UCHII region the ionized gas has full velocity extent $\sim 40\ \text{km s}^{-1}$; in addition the three UCHII regions are offset from each other in velocity by $\sim 10\ \text{km s}^{-1}$, peaking at $\sim +33$ and $\sim +23\ \text{km s}^{-1}$. The ionized

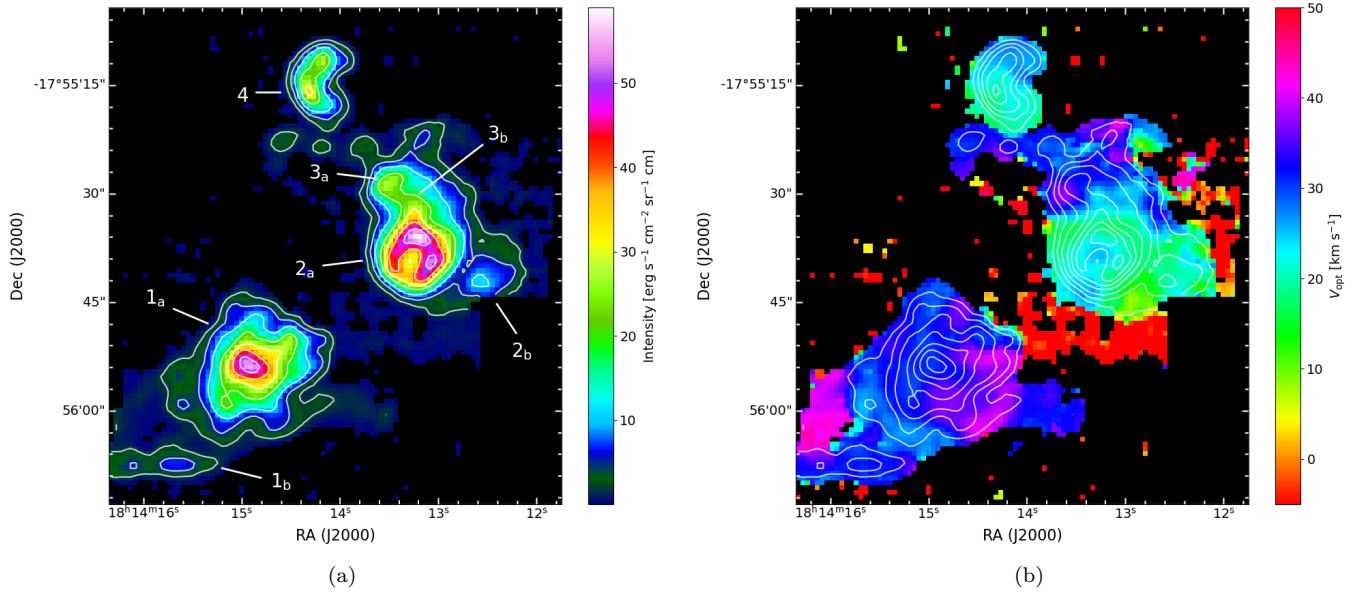


Figure 1. W33 Main [NeII] data cube (a) 0th Moment Map showing the total [NeII] emission intensity, labelled with the names assigned the sub-sources. (b) 1st moment of the data cube showing the weighted average velocity in color and the total intensity in contours. The maps have ~ 1.4 arcsec spatial resolution and 4 km s^{-1} kinematic resolution. Contour levels are $[2, 5, 10, 20, \dots, 50] \text{ erg s}^{-1} \text{ cm}^{-2} \text{ sr}^{-1} \text{ cm}$.

gas integrated over the entire W33 Main region peaks at velocity $\sim +29 \text{ km s}^{-1}$. These UCHII regions have previously been detected in the IR and radio continuum, and the source identifications in the radio and infrared have not been consistent; the infrared sources were numbered from west to east as IRS1,2,3 and the radio continuum sources labelled as A,B,C from north to south. We show on Figure 1 the labels we use throughout the paper, which correspond to the infrared labels of Beck et al. (1998) as W33M1 (IRS 1), W33M2+3 (IRS 3) and W33M4 (IRS 2). Note that the UCHII regions are not uniform but hold sub-structures and sub-sources that appear both in the intensity distribution and as velocity features; these are identified and labelled in the figure. Figure 11 shows the total [NeII] emission map overlaid on the 6 cm radio map of Haschick & Ho (1983). This map shows that the ionized gas traced by [NeII] emission agrees with the radio continuum extremely well except for a diagonal band across the centre where there is radio continuum but no [NeII]. We believe this band to show where more H II regions are so deeply embedded in the cloud that even the [NeII] is obscured; this feature is also seen in the Spitzer $8 \mu\text{m}$ image of the region (Churchwell et al. 2009).

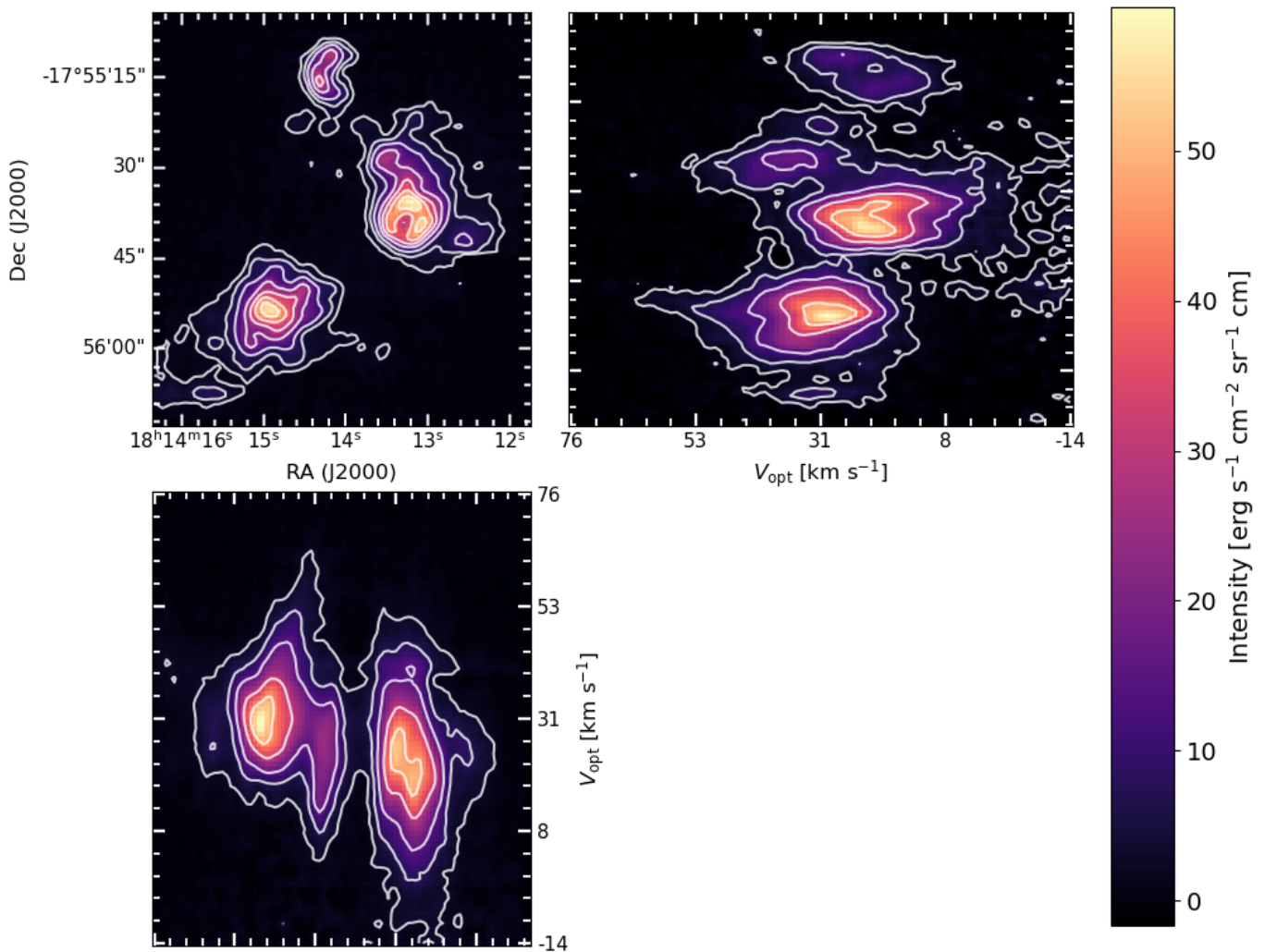


Figure 2. W33 Main [NeII] data cube composite showing the 0th moment maps along the spectral axis (top left), RA axis (top right) and Dec axis (bottom). The maps have 1.4 arcsec spatial resolution and 4 km s^{-1} kinematic resolution. Contour levels are [2,5,10,20,30,40,50] $\text{erg s}^{-1} \text{cm}^{-2} \text{sr}^{-1} \text{cm}$.

3. METHODOLOGY

3.1. [NeII] as Tracer of Ionized Gas

We use [NeII] as a tracer of the total ionized gas and assume that the ratio of [NeII] line intensity to the ionized gas emission measure is constant over the entire W33 Main region. For this to be valid the gas-phase abundance of neon and the fraction of neon in Ne^+ must be constant across W33 Main and the gas densities well below the critical density $n_c = 3.6 \times 10^5 \text{ cm}^{-3}$ (Lacy, Beck, & Geballe 1982) at which quenching is significant; all these statements are consistent with previous work on W33 (constant neon abundance is discussed in (Beck et al. 1998)). We further assume that the extinction at $12.8 \mu\text{m}$ is constant over the UCHII regions we model, consistent with the radio maps and the $8 \mu\text{m}$ Spitzer images.

3.2. Two Models of Cometary Structure in UCHII Regions

Two primary mechanisms for creating complex UCHII region structures are density gradients in the surrounding cloud and the motion of the exciting star through the gas. Zhu et al. (2015) present hydrodynamical models showing

that the 'cometary' structure observed for many UCHII regions can be created by a stationary star in an exponential density gradient. Their model of 'champagne flow' is based on an exciting star which is stationary and close to the near face of the embedding cloud and predicts that gas in the 'tail' of the cometary structure will be blue-shifted relative to the head as the gas flows out of the cloud. We will discuss this model further below in connection with W33M2, the most champagne-flow like of the sub-sources. The other sources in W33 Main do not show such clear cometary behavior; instead their appearance and kinematics suggest that exciting stars are moving through the cloud and creating bow shocks. In the next section we review bow-shock models and how we use them in this paper.

3.2.1. Bow Shock Models

Bow shocks are of fundamental importance in UCHII regions and we here review how they will appear in the simulations. When a massive star with a stellar wind moves supersonically in a medium it creates a bow-shock (Wood & Churchwell 1989a; Mac Low et al. 1991; Van Buren & Mac Low 1992; Mackey et al. 2015): the stellar wind and ambient material collide to form a shocked region in front of the star which is stationary in the frame of the star and approximately paraboloidal in shape (Wilkin 1996). The bow shock creates very dense neutral material that potentially traps the expanding ionization front and halts its expansion towards the front; this over-pressure depends on the velocity of the star.

Embedded stars moving through the dense ambient cloud are expected to create bow shocks. Bow shocks can produce the cometary, core-halo, and shell structures which are the most common morphologies of UCHII regions, and prolong the lifetime of the UCHII stage. The precise form taken depends on the ambient density, stellar velocity, nature of the stellar wind and the angle of observation; all these parameters need careful tuning to match the observations (Churchwell 2002).

3.3. Hydrodynamics - PLUTO

We created the models of the UCHII regions with the PLUTO hydrodynamics package (Mignone et al. 2007). All the UCHII region simulations were run inside a $256 \times 256 \times 256$ 3D Cartesian grid so that each grid cell was 0.0013 parsec across and the boundary conditions in all directions were set to outflow. The Navier-Stokes equations of classical fluid dynamics were solved in an Eulerian method in 3D Cartesian coordinates using a HLL approximate Riemann solver (Harten, Lax, & Leer 1983). $T_e = 10^4 K$ was assumed, heating and cooling were not included, and a Courant number of 0.3 was used based on the Courant–Friedrichs–Lewy condition (Courant, Friedrichs, & Lewy 1967).

Each star starts with a spherically symmetric radial wind flowing from the origin of coordinates and moves through an ambient medium of constant density at stellar speed v_* in the \hat{j} direction. This gives initial conditions:

$$\rho = \rho_a \quad p = p_a \quad \mathbf{v} = v_* \hat{j} \quad (1)$$

The wind is injected within the internal boundary r_0 (inside the inner reverse shock of a stellar wind bubble) and based on Mignone (2014) maintains these flow quantities constant in time:

$$r^2 v_r \rho = r_0^2 V_0 \rho_0 \quad v_r = V_0 \tanh\left(\frac{r}{r_0}\right) \quad p = \frac{c_s^2}{\Gamma} (\rho_0^{1-\Gamma}) \rho^\Gamma \quad (2)$$

where r is the radius, ρ_0 is the ambient density, V_0 is the gas velocity at r_0 , p is the gas pressure, c_s is the sound speed of the gas and $\Gamma = c_P/c_V$ is the ratio of specific heat coefficients. We note that r_0 was set to a distance of between 3 and 6 cells from each star according to its appropriate mass, so that the effect of the stellar wind is captured at a sufficient resolution for our models; for a single star, increasing the resolution by a factor of 4 didn't change the various shock radii, the only major difference was that Rayleigh-Taylor instabilities developed at the forward shock radius because of the large density gradient (Meyer et al. 2014), however this would have a negligible effect on our results, especially for the interactions of multiple star trails, and therefore wouldn't affect the fine-tuning of the stellar parameters. We note that at much longer timescales these approximations can lead to significant discrepancies from analytical models of stellar wind bubbles (Pittard et al. 2021) With dimensions such that the spherical wind shell maintains $r_0 = V_0 = \rho_0 = 1$ the effects of increasing stellar velocity are shown in Figure 3. The stationary star creates a Strömgren sphere but forms a cometary tail when moving supersonically. The faster the star moves, the more elongated the cometary shape and the greater the ram pressure at its apex.

The trail remains imprinted on the medium for some time tracing the star's movement, and when the stellar trajectory is not a straight line the result is a short curled tail. An example of the curled tail left behind by the circular motion of

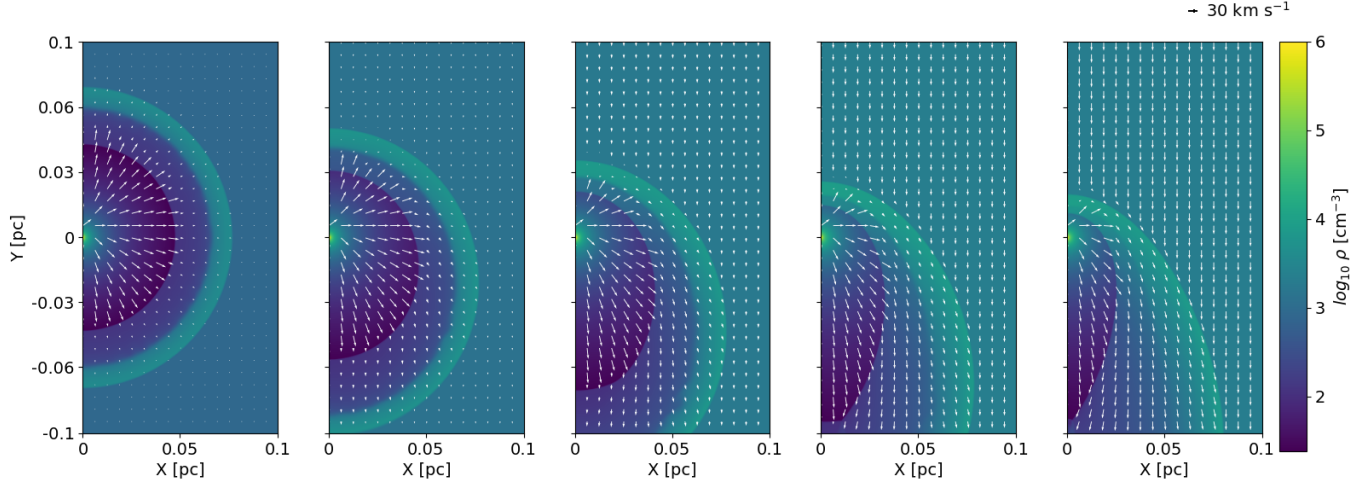


Figure 3. Density plots, in axisymmetric cylindrical coordinates in the star’s frame of reference and with the star at the origin, of the cometary shape formed when the stellar wind interacts with the ambient material for a moving B0V star. The cometary shape becomes more elongated with increasing stellar velocity from 0 km s⁻¹ (far left) to 30 km s⁻¹ (far right).

a B0V star moving at 20 km s⁻¹ can be seen in Figure 4. Similar structures are seen in density maps from simulations of the interaction between the stellar winds of two stars (van der Helm et al. 2019), and observed in the environment of the evolved star Mira (Martin et al. 2007). The similarity to the observed data cube motivated us to model the W33 UCHII regions by combining multiple stars, each with a wind and curved trajectory.

We assumed that the stellar orbits are circular in x, y and that within one UCHII region the stellar orbits are co-planar. Therefore, each star in orbital motion moves on a curve described by

$$x = x_0 + r_{\text{orb}} \cos(\omega_{\text{orb}}t + \varphi_{\text{orb}}) \quad y = y_0 + r_{\text{orb}} \sin(\omega_{\text{orb}}t + \varphi_{\text{orb}}) \quad z = z_0 + z_{\text{vel}}t \quad (3)$$

where (x_0, y_0, z_0) is initial position of each star, z_{vel} is the stellar velocity and r_{orb} , ω_{orb} and φ_{orb} are respectively the orbit’s radius, circular velocity and phase.

We wrote a 3D visualization program that allowed us to modify wind, orbit and stellar parameters for each star so as to duplicate the morphology of each UCHII region in the data cube. The adjustable parameters and the best value we found for every star are shown in Table 1. In Figures 5, 7 and 9 we show 3-dimensional views of the best model stars and their trajectories, as well as of the original data cube. As part of the fine-tuning process we determined the ratio between the inner reverse shock radius and the radius of the shocked ambient gas, and used this with the formulae of Weaver et al. (1977) to derive the spectral type, mass and temperature of each star. We assumed OB star values of (Lamers & Leitherer 1993; Krtićka 2014) and that the UCHII region had been expanding for $\sim 10^3 - 10^4$ yr.

3.4. 3D Ionic Line Emission Profile Simulation - RADMC-3D

The PLUTO outputs (Ne⁺ density, velocity and position) were input to the radiative transfer software RADMC-3D (Dullemond et al. 2012) which calculated the 3D [NeII] line profile emission. We assumed constant gas temperature 10⁴K. The line profile for each UCHII region in W33 Main was simulated separately at the spectral range and resolution matching the observed [NeII] data cube. However the zero point of the velocity scale in the simulations was chosen for computational convenience, and is not the velocity of the W33 cloud, so the velocities displayed for the simulation results are relative only. When the original data is presented, the velocities are the observed values.

4. SIMULATION RESULTS

In this section we show the results of the 3D hydrodynamic and line profile simulations, fine tuned to match each UCHII region. Since the simulations are on a 0.6 arcsec grid we convolve the results with a Gaussian to create an effective PSF (point spread function) of 1.4 arcsec, matching that of the observations, and compare them to the original

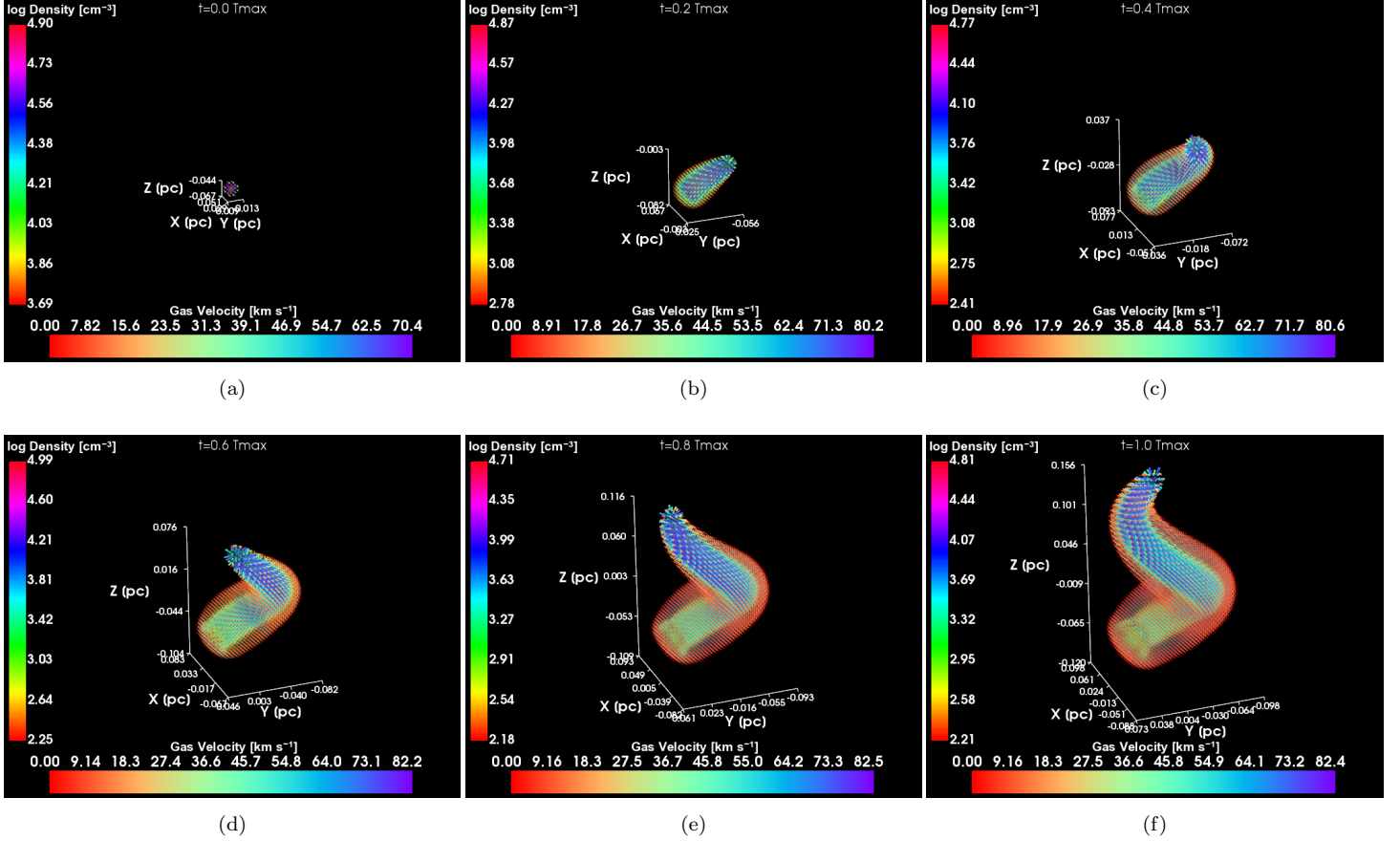


Figure 4. Example of the curled tail that is left behind, at multiple timesteps, by a B0V star performing a complete orbit and moving at 20 km s^{-1} in the Z+ axis direction with orbital parameters perpendicular to the Z axis of: $r_{\text{orb}} = 0.040 \text{ pc}$, $\omega_{\text{orb}} = 2.03 \times 10^{-11}$ and $\varphi_{\text{orb}} = 0 \text{ rad}$.

data cube. We now present, for each sub-source, the original data and the locations and trajectories of the stars which produce the best fit. We then compare the kinematics and structure of the simulated model and the original data in the form of channel maps and position-velocity diagrams (PVDs). In section 5 we discuss and check the results in the context of star formation models.

4.1. *W33 Main 1*

W33M1 (W33 Main 1) includes W33M1_a which has an irregular morphology and W33M1_b which is much smaller and has a cometary form. The clues for the trajectories of stars and ionized gas clumps in W33M1_a are subtle. Using our visualization program to fine-tune the models we have determined the extent and shape of each separate inner star clump and display the curve of its orbit. The simulations best fitting the data, shown in Figure 5, have W33M1_b as a single star and W33M1_a with as many as 7; 3 stars closer to the centre and the rest in the outer parts. Note that some of these may be hot dense gas clumps which are distinct in the data cube but may not hold massive stars.

Figure 6 compares the original data and model results for W33M1. The channel maps of the simulation results agree with the original data in overall structure: there is a central peak surrounded by smaller clumps. The simulations have a more organized appearance; the secondary clumps are stronger and more defined than in the original data. The PVDs taken from the data and the simulations also agree on large scales, with a concentrated central source and a spatially extended high velocity ‘tail’ in both RA and Dec. The PVDs from the simulated data have more pronounced small-scale structure: specifically, the high velocity tail in the simulations is clearly split into two separate spatial branches, a feature which is present but much less clearly so in the original data. The tendency of the secondary features to be more pronounced in the simulations than in the original data suggests that some non-stellar density

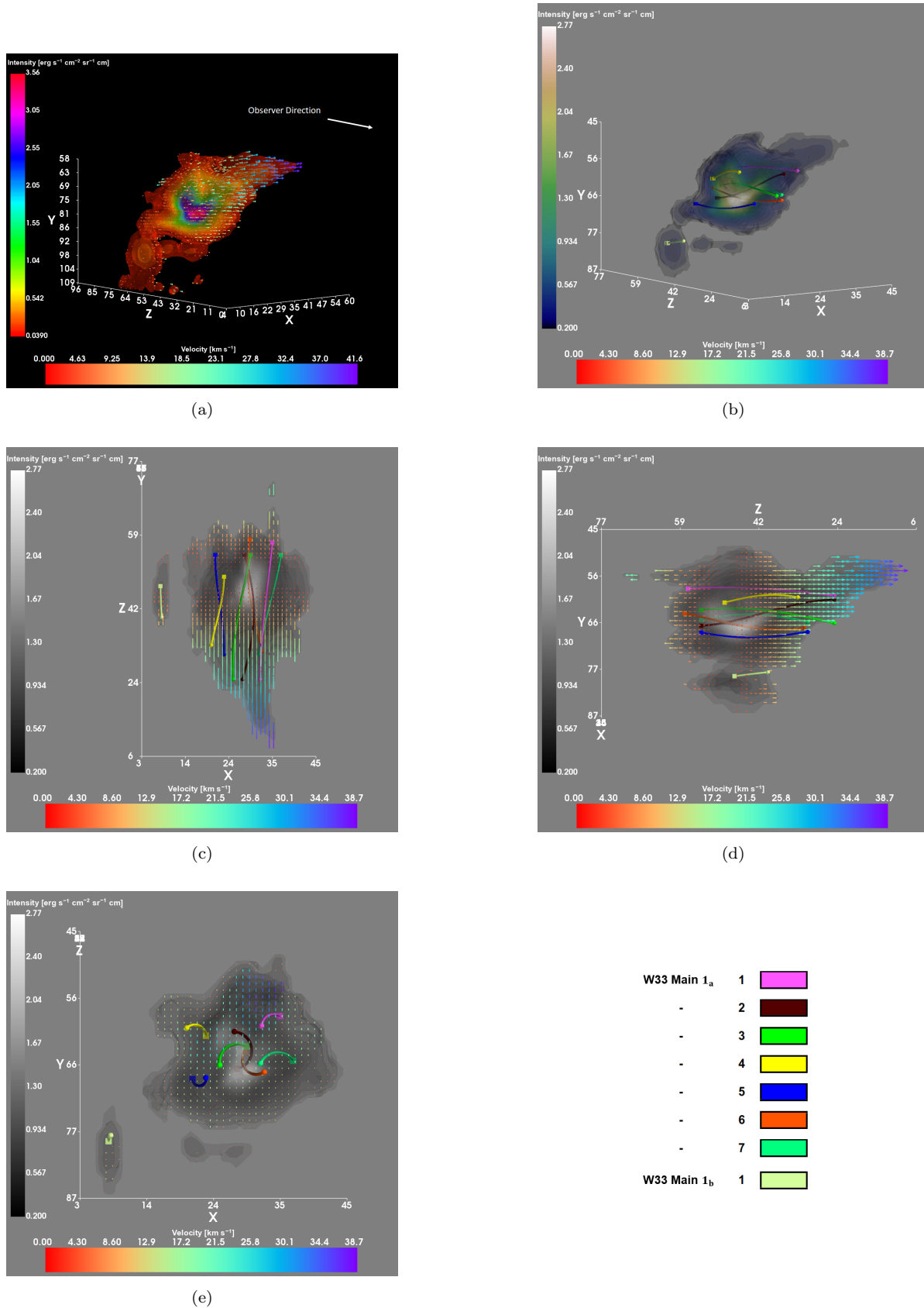


Figure 5. 3D View of the original [NeII] data cube cropped to the volume containing W33 Main 1 with the colored star movement curves (legend on bottom right) from 3 axes directions (Z- is the observer direction): (a) Dec, (b) RA, (c) Spectral/Kinematic. The X,Y,Z units are as follows: X axis is RA (1 X Unit = 0.66 arcsec), Y axis is Dec (1 Y Unit = 0.05s) and Z axis is spectral/kinematic axis (1 Z Unit = 1 km s⁻¹). The velocity axis is also denoted by the colored arrows where only the absolute velocity is considered. Each star curve shows the movement of a single star starting from the sphere shape and ending with the cube shape.

Table 1. PLUTO Stars and Movement Parameters

UCHII Region	Star #	Spectral Type	M_* [M_\odot]	T_*^{eff} [K]	v_* [km s $^{-1}$]	r_0 [10^{-3} pc]	V_0 [km s $^{-1}$]	r_{orb} [pc]	ω_{orb} [10^{-12} s $^{-1}$]	φ_{orb} [rad]
W33 Main 1 _a	1*	B1.5V	9.26	24000	24.12	4.26	40	0.014	6.75	1.05
-	2	B0.5V	12.69	28000	21.93	6.39	60	0.021	9.33	4.97
-	3	B0.5V	12.69	28000	21.93	6.39	60	0.020	7.58	1.05
-	4*	B1.5V	9.26	24000	12.06	4.26	40	0.013	7.65	0.05
-	5*	B1V	10.88	26000	17.54	4.79	45	0.007	11.26	3.12
-	6	B0.5V	12.69	28000	19.74	6.39	60	0.016	9.33	2.48
-	7*	B1V	10.88	26000	17.54	4.79	45	0.021	7.00	0.61
W33 Main 1 _b	1	B1.5V	9.26	24000	5.48	3.19	30	0.011	2.10	3.14
W33 Main 2 _a	1	B1V	10.88	26000	21.93	5.32	50	0.015	10.12	5.29
-	2	B1V	10.88	26000	19.74	5.32	50	0.021	9.33	0.87
-	3	B1V	10.88	26000	21.93	4.79	45	0.037	9.33	3.21
-	4	B1.5V	9.26	24000	19.74	4.26	40	0.018	9.33	6.16
-	5	B1V	10.88	26000	15.35	4.79	45	0.016	5.83	0.38
W33 Main 2 _b	1	B1.5V	9.26	24000	4.24	4.26	40	-	-	-
W33 Main 3 _a	1	B1.5V	9.26	24000	8.22	3.19	30	-	-	-
W33 Main 3 _b	1	B1.5V	9.26	24000	5.48	3.72	35	-	-	-
W33 Main 4	1	B1.5V	9.26	24000	7.89	4.26	40	0.021	5.83	0.00
-	2	B1.5V	9.26	24000	10.53	3.72	35	0.005	19.83	0.52

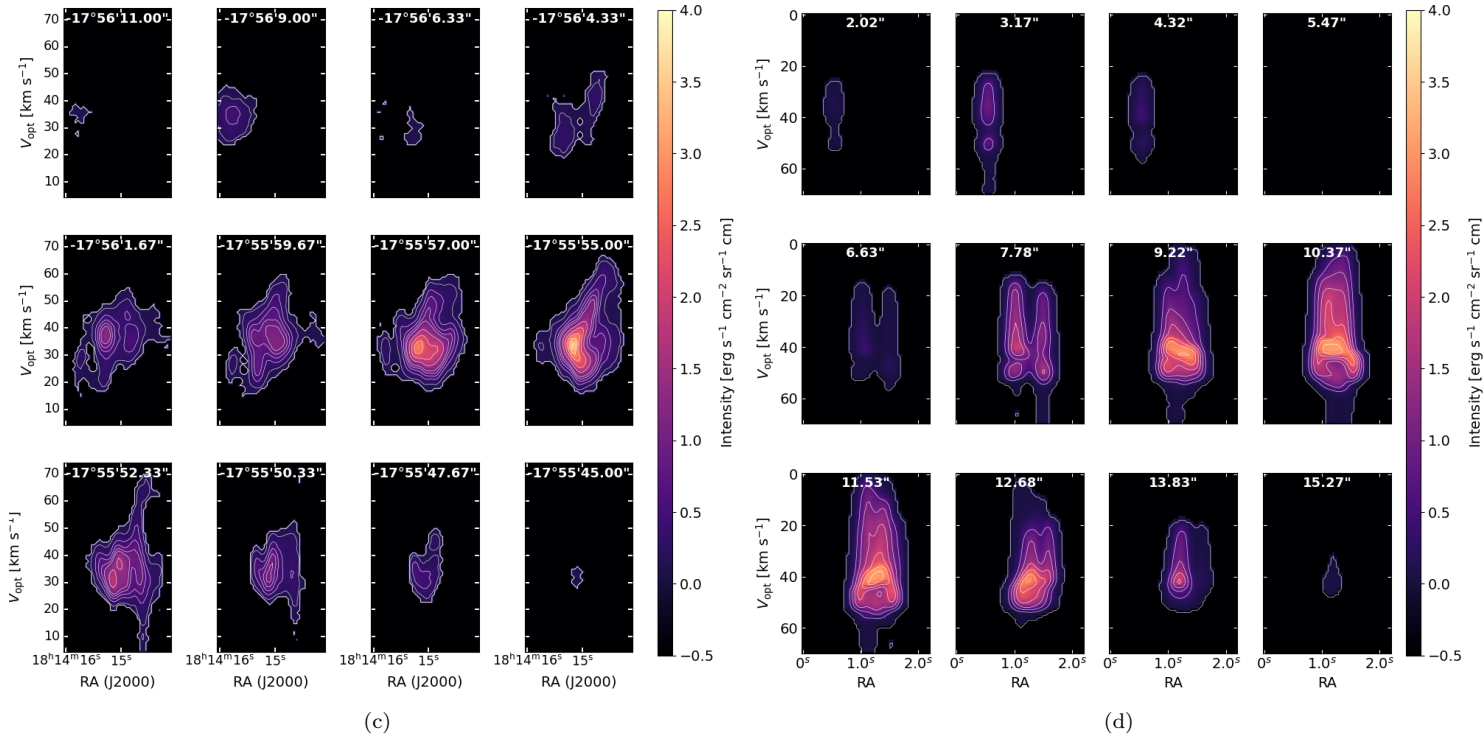
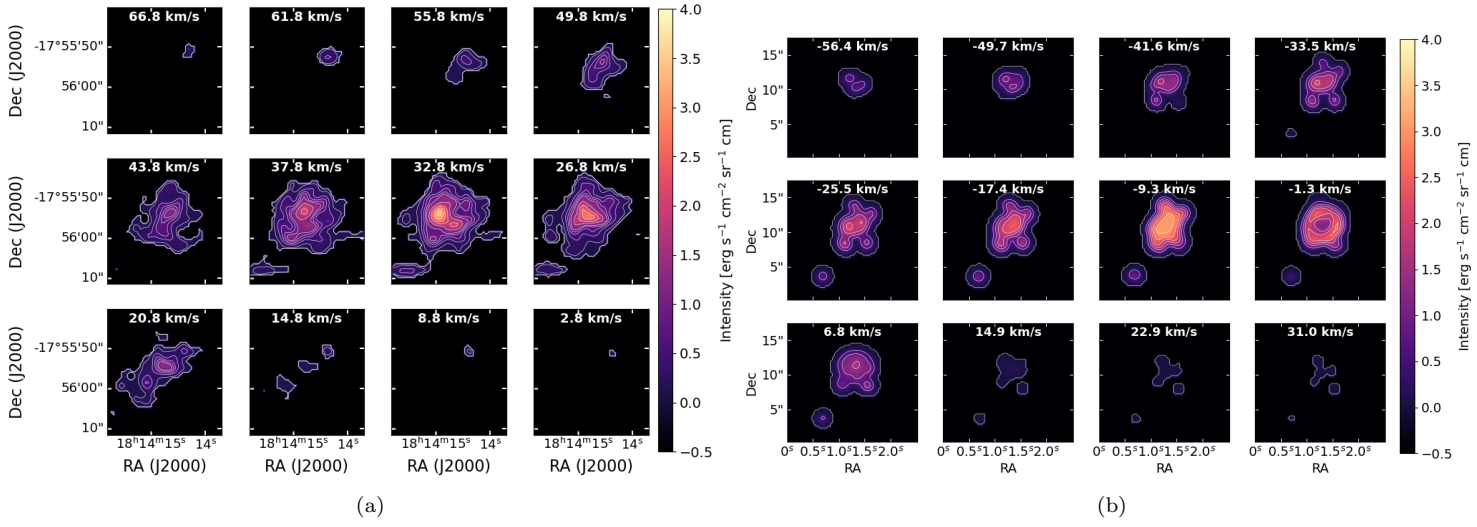
NOTE— List of stars simulated within each UCHII region. Stars marked with '*' are potentially simple gas clumps. For each star its listed parameters include mass (M_*), effective temperature (T_*^{eff}), velocity relative to the ambient material (v_*), internal boundary of its stellar wind bubble (r_0), V_0 is the gas velocity at r_0 , orbital movement radius (r_{orb}), angular velocity (ω_{orb}) and phase angle (φ_{orb}). Note that these orbital parameters do not describe the physical orbit but refer to the circular paths of the simulations which approximate the star's relative movement.

structures may have been modelled as OB stars. We note that the morphology of W33M1_a is not easily reproduced. Further fine-tuning of the stellar motion curves may improve the correspondence.

4.2. W33 Main 2 + 3

Examination of the data cube shows that W33M2 and W33M3 are moving in opposing directions and grazing each other in a partial collision. We therefore treat them together in our simulations. Figure 7 shows that W33M2_a, W33M2_b, W33M3_a and W33M3_b all appear somewhat cometary in morphology. W33M2_a is particularly clear because it appears that our observations look directly into the tail, and that the tail gas is expanding out of the cloud towards us, as shown by the blue-shift of the tail relative to the rest of the cloud. W33M2_a may fit the picture of a pure champagne flow UCHII region and this model is presented in the Discussion section on this source. We here treat both W33M3, which does not have the same kinematic signature of gas expansion, and W33M2 as comprising moving stars and bow shocks. In this picture we model the complex triple tail internal structure of W33M2_a, shown in Figure 7, as tracing the intertwining of multiple stellar orbits. The simulations suggest that W33M2_a includes 4 stars orbiting each other in a quaternary system (Star #1-4) and one whose membership in the system is unclear (Star #5), and that each of W33M3_a, W33M3_b and W33M2_b hold one star.

In Figure 8 we compare channel maps and PVDs of the original data on W33M2 and W33M3 to the simulations. The channel maps show reasonable agreement of the simulation results and the original data cube; both simulations and data show a ring with secondary clumps that peak at different velocities. As we saw for W33M1 the secondary features are more defined in the model than in the original data. In both the data and the simulations, PVDs in both dimensions display two bright 'arms', spatially distinct and extended in velocity, that join at a 'head' to form the bow shock, the shock appearing in the PVDs as a region of steep contours, and a spatially distinct tail extending to blue velocities. The simulated PVDs however are 'clumpier' than the original data, which is notably smooth. The 'clumps'



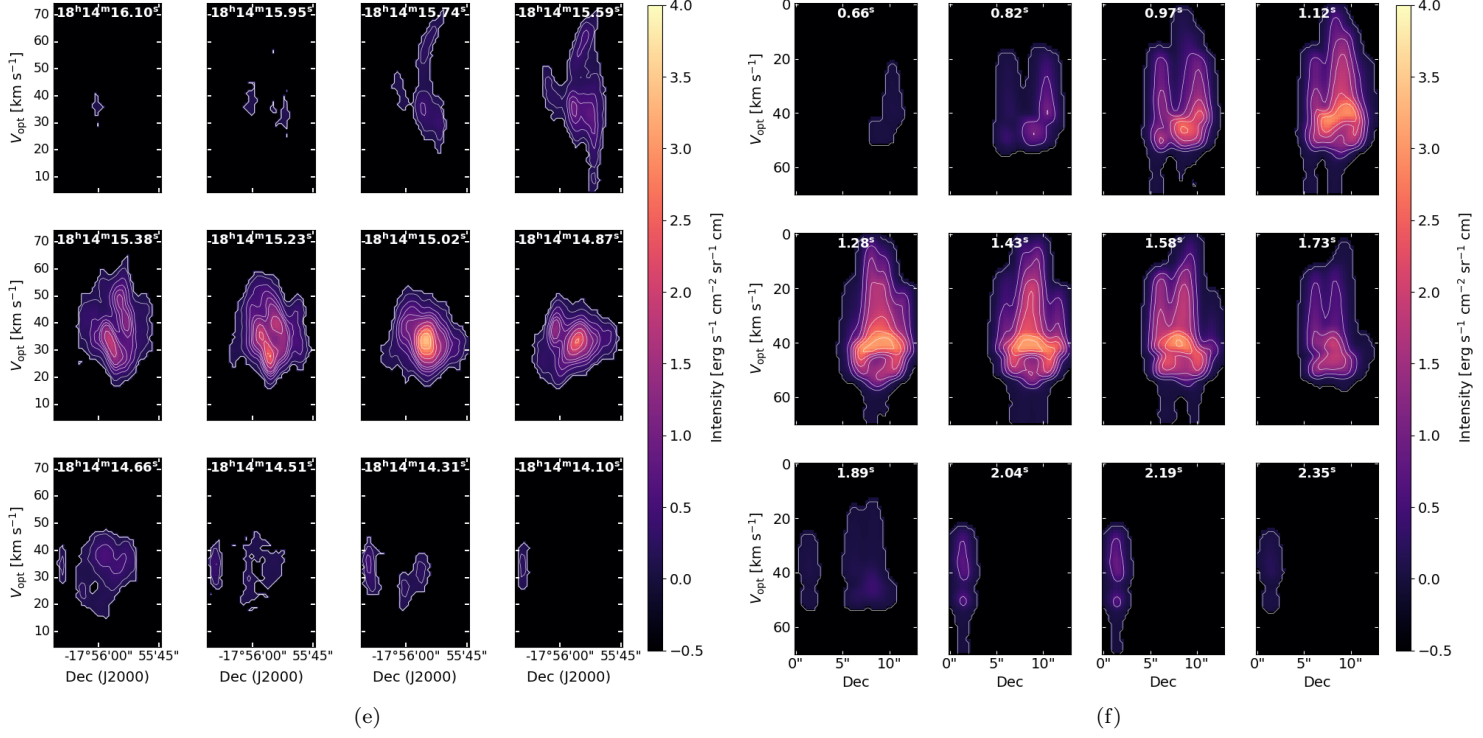


Figure 6. Comparison of original data cube and the simulation results for W33 Main 1: Channel maps of (a) the W33 Main [NeII] data cube cropped with contour levels at [0.05, 0.1, 0.2, 0.4, 0.6, 0.8, 1.0, 1.5, 2, 2.5, 3] $\text{erg s}^{-1} \text{cm}^{-2} \text{sr}^{-1} \text{cm}$ and (b) line profile emission simulation results with contour levels at [0.0, 0.5, 1, 1.5, 2, 2.5, 3.0, 3.3, 3.5, 3.7, 4.0] $\text{erg s}^{-1} \text{cm}^{-2} \text{sr}^{-1} \text{cm}$. (c) Position-Velocity Diagrams of W33 Main 1 in RA from the original data and (d) from the simulation. (e) Position-Velocity Diagrams of W33 Main 1 in Dec from the original data and (f) the simulations.

in space and velocity show the presence of the multiple exciting stars assumed in this model; the relative smoothness of the original data may argue that fewer or only one star is present.

4.3. W33 Main 4

W33M4 has the simplest structure of the UCHII regions: the radio measurements (Beck et al. 1998) were consistent with a single embedded star. The shape of W33M4 suggests a cometary UCHII region seen sideways but the kinematics do not agree: the data shows two clumps offset in velocity by $\sim 10 \text{ km s}^{-1}$ with some interaction between them. We found the the best fit to be a binary pair in an orbit at about $\sim 30^\circ$ relative to the observer. The stellar trajectories are shown in Figure 9(c,d,e).

In Figure 10 we show the results of the hydrodynamic and radiative simulations in 3D for W33M4. The channel maps of the simulations agree fairly well with the data. Both the original and simulated PVDs show two sources, offset in velocity by $\sim 10 \text{ km s}^{-1}$ and each extending $\sim 20 \text{ km s}^{-1}$; interaction and overlap between the two is more apparent in the simulations than in the original data.

5. THE SIMULATED STELLAR POPULATION AND MASS FUNCTION

Our simulations propose multiple stars for each UCHII region in W33 Main. These stars, and their trajectories, are shown in in Figure 11 overlaid on the 0th moment maps of the original data cube and the 6cm radio map from Haschick & Ho (1983); the models and the data agree spatially and kinematically. The deduced stellar masses are all of early B type. These are later than the stellar types quoted by Beck et al. (1998), but there are substantial uncertainties and possible degeneracies in their derivation of stellar type from infrared line ratios. Table 1 shows that there are more stars in the lower mass than the high mass ranges, as predicted by all normal IMFs (initial mass function), but the number of stars is too small and the mass range covered too narrow for us to derive a meaningful exponent α for the local IMF. The total ionizing flux of the simulated UCHII regions is compared to the original data cube in Figure 12; most of the simulated UCHII regions slightly exceed the original in flux. The simplest explanation of this discrepancy

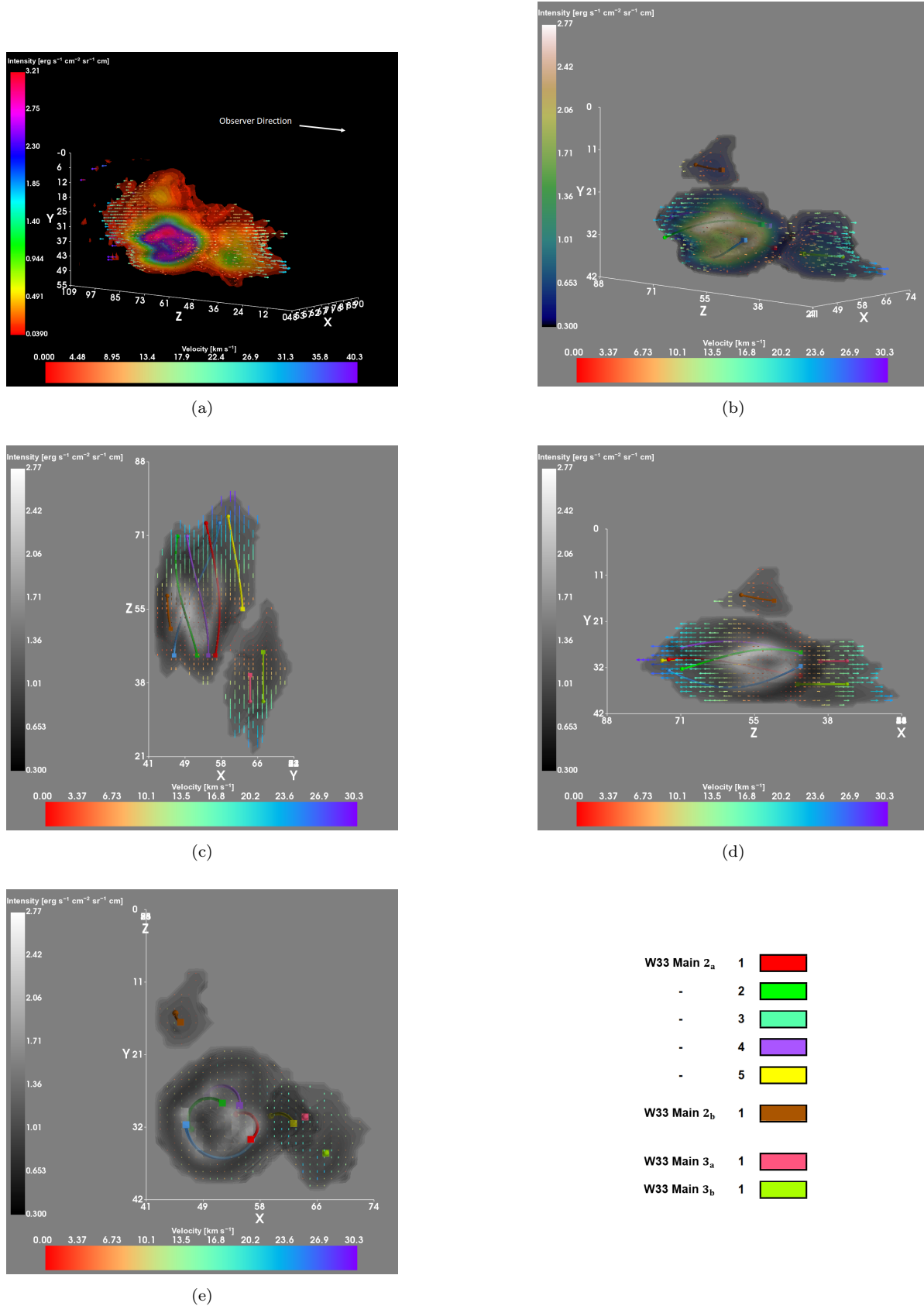
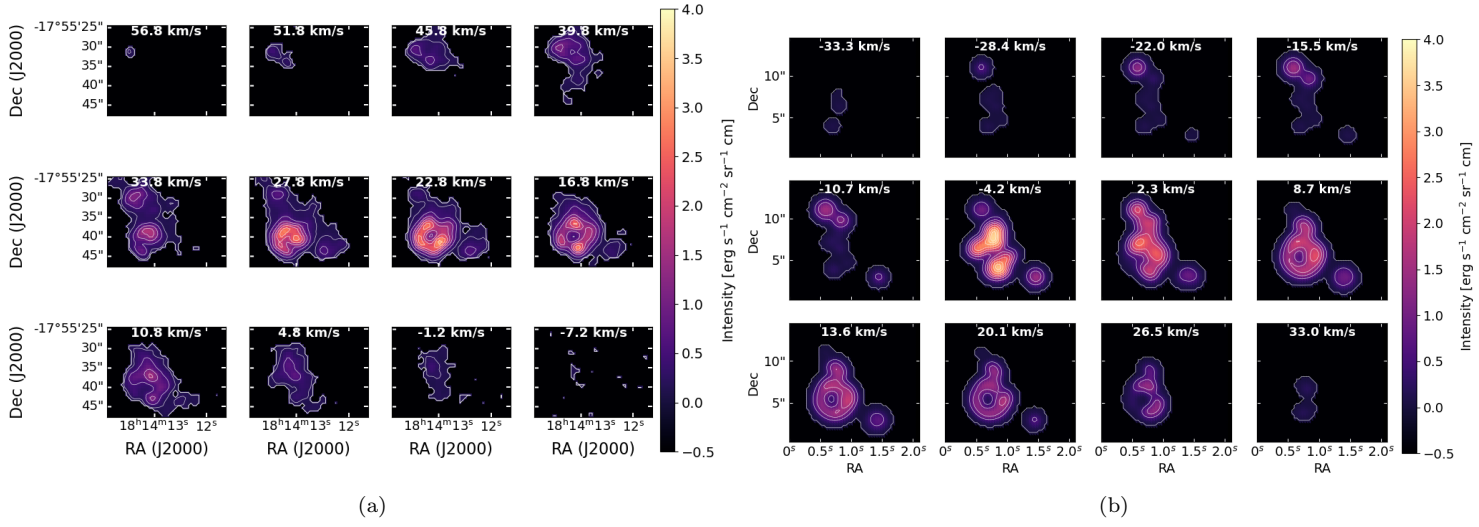
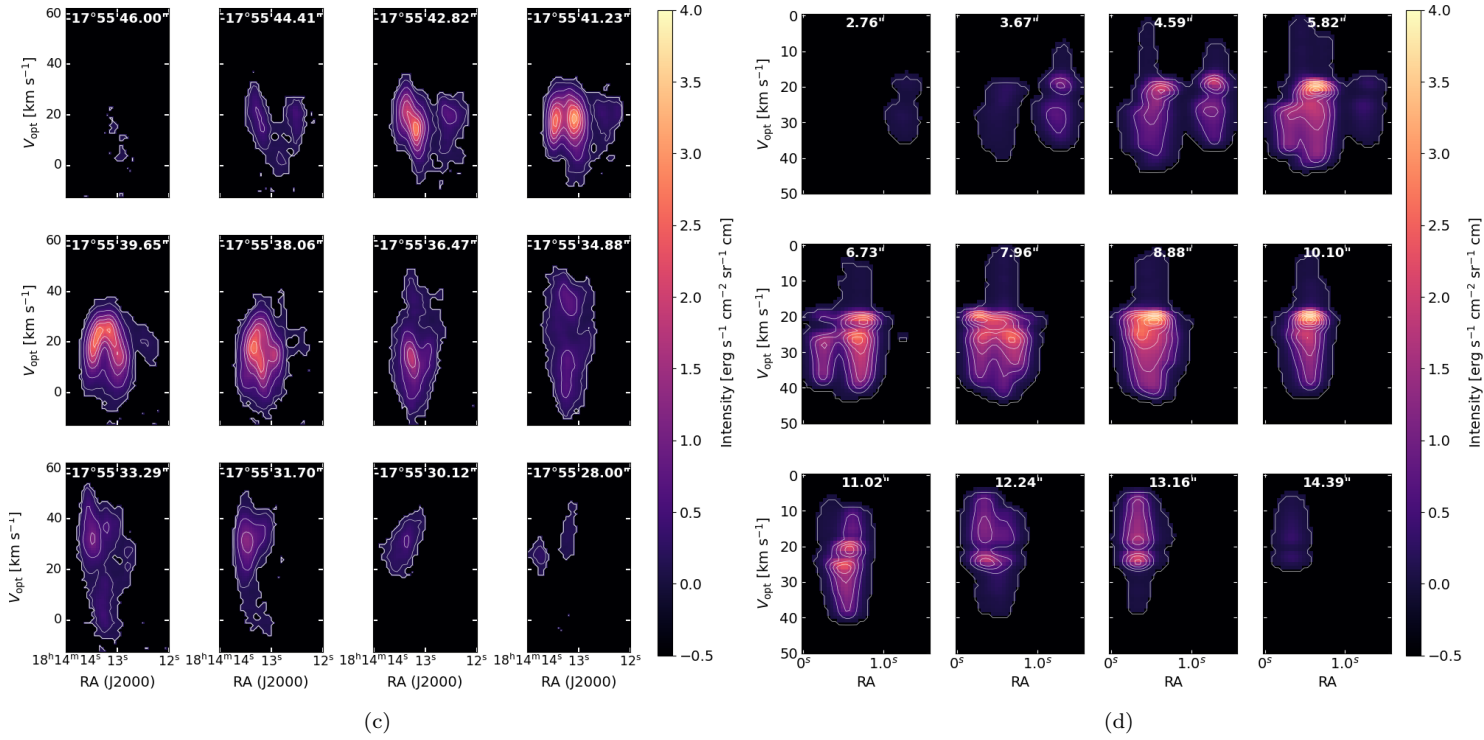


Figure 7. 3D View of the original [NeII] data cube cropped to the volume containing W33 Main 2+3 with the colored star movement curves (legend on bottom right) from 3 axes directions (Z- is the observer direction): (a) Dec, (b) RA, (c) Spectral/Kinematic. The X,Y,Z units are as follows: X axis is RA (1 X Unit = 0.66 arcsec), Y axis is Dec (1 Y Unit = 0.05s) and Z axis is spectral/kinematic axis (1 Z Unit = 1 km s⁻¹). The velocity axis is also denoted by the colored arrows where only the absolute velocity is considered. Each star curve shows the movement of a single star starting from the sphere shape and ending with the cube shape.



(a)

(b)



(c)

(d)

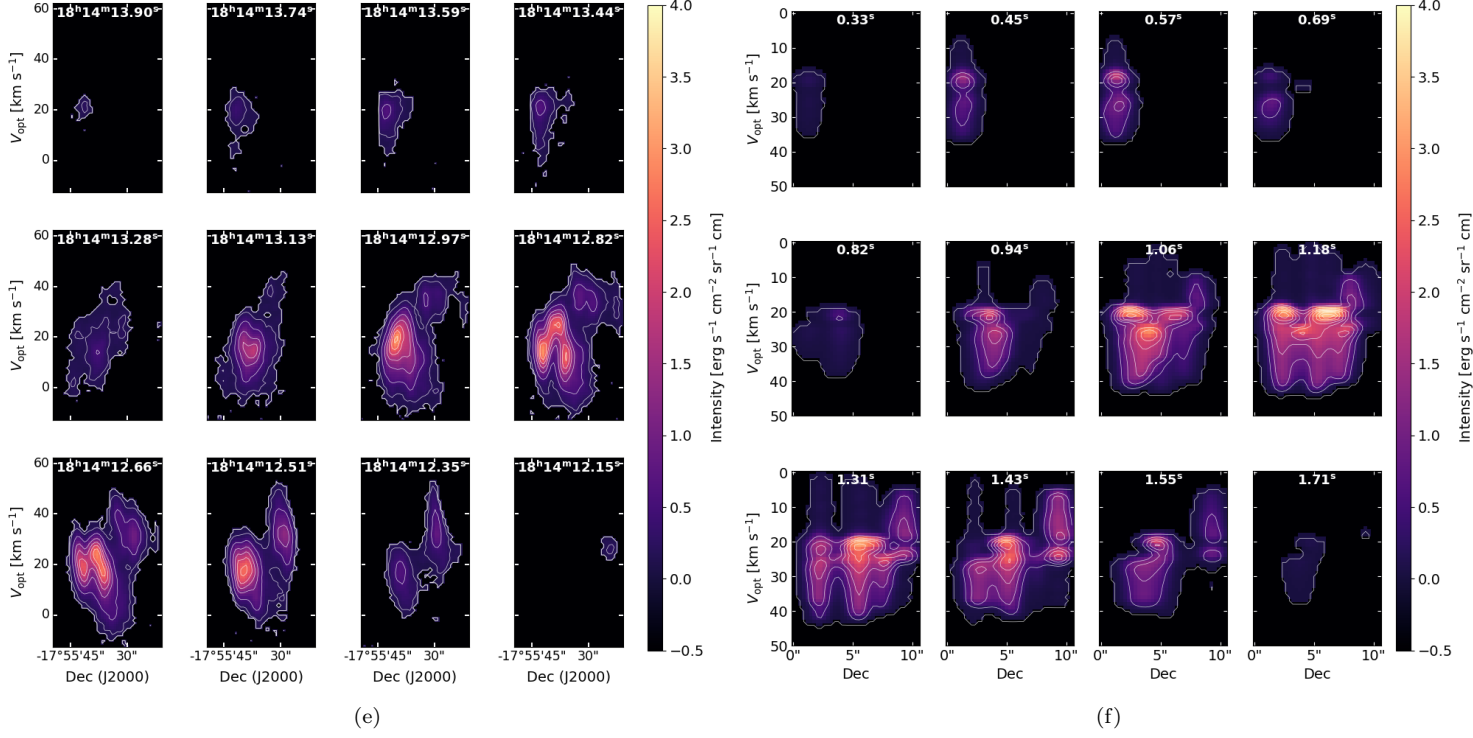


Figure 8. Comparison of original data cube and simulation results for W33 Main 2+3: Channel maps of (a) W33 Main [NeII] data cube cropped with contour levels at [0.05, 0.1, 0.2, 0.5, 1.0, 1.5, 2, 2.5, 3] $\text{erg s}^{-1} \text{cm}^{-2} \text{sr}^{-1} \text{cm}$ and (b) Line profile emission simulation results with contour levels at [0.0, 0.5, 1, 1.5, 2, 2.5, 3.0, 3.3, 3.5, 3.7, 4.0] $\text{erg s}^{-1} \text{cm}^{-2} \text{sr}^{-1} \text{cm}$. Position-Velocity Diagrams in RA from the data cube (c) and the simulations (d), Position-velocity Diagrams in Dec from the data cube (e) and the simulations (f).

is that some of the 'stars' whose trajectories appear in the models are not true OB stars but dense clumps whose embedded stars, if any, are not ionizing.

Are the high numbers of stars suggested by our simulations realistic? In the empirical limit of high-mass star formation, proposed by [Kauffmann et al. \(2010\)](#), the number of stars in each UCHII region can be predicted from the total mass in a molecular clump:

$$m(r) > 870M_{\odot} \left(\frac{r}{\text{pc}} \right)^{1.33} \quad (4)$$

In Table 2 we compare this prediction to the simulations. The predicted and simulated stellar populations agree with the exception of W33M1_a, another indication that some of the proposed stars in W33M1_a are not true stars.

6. CONCLUSIONS AND DISCUSSION

This paper reports on simulations of the UCHII regions of W33 Main which were motivated by the goal of explaining high resolution data on the ionized gas. We have obtained a [NeII] $12.8 \mu\text{m}$ data cube of W33 Main with 1.4 arcsec spatial and $\sim 5 \text{ km s}^{-1}$ velocity resolution; this velocity resolution is a crucial advantage over HI line measurements which are limited by thermal broadening to $\gtrsim 21 \text{ km s}^{-1}$. Unlike most earlier work on UCHII regions which assumed single massive stars in each source, our simulations are based on the picture that each UCHII may contain several smaller ionizing stars, and that the bow shocks of these stars and their relative motions can create the complicated gas distributions and velocity features that are observed. Our simulations include visualizations that permit us to fine-tune the stellar trajectories to match the spatial and kinematic effects observed. We found that:

- The structures and kinematics observed for these UCHII regions cannot, with the one exception of W33M2_a, be satisfactorily modelled by a single embedded star either moving or stationary.

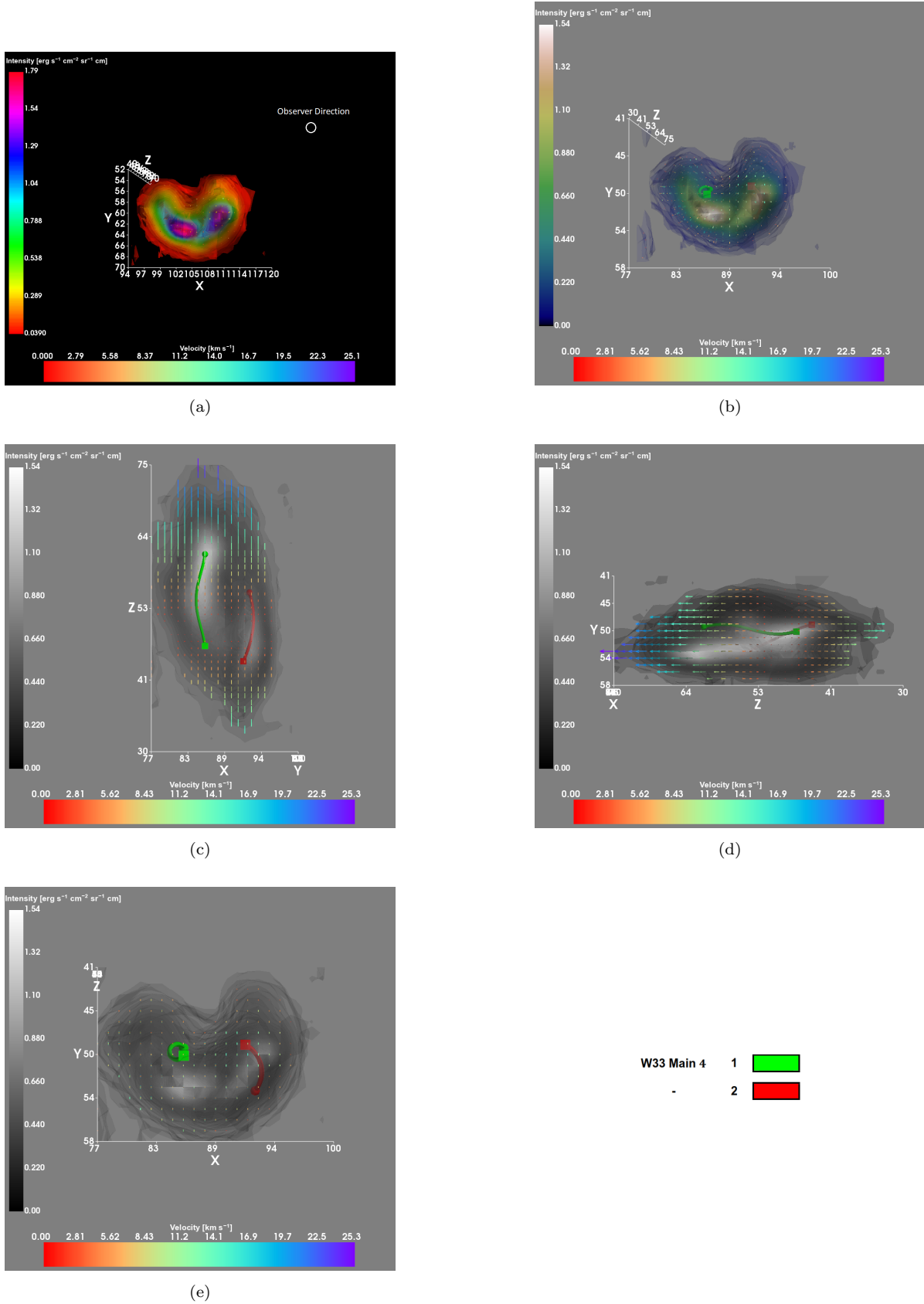
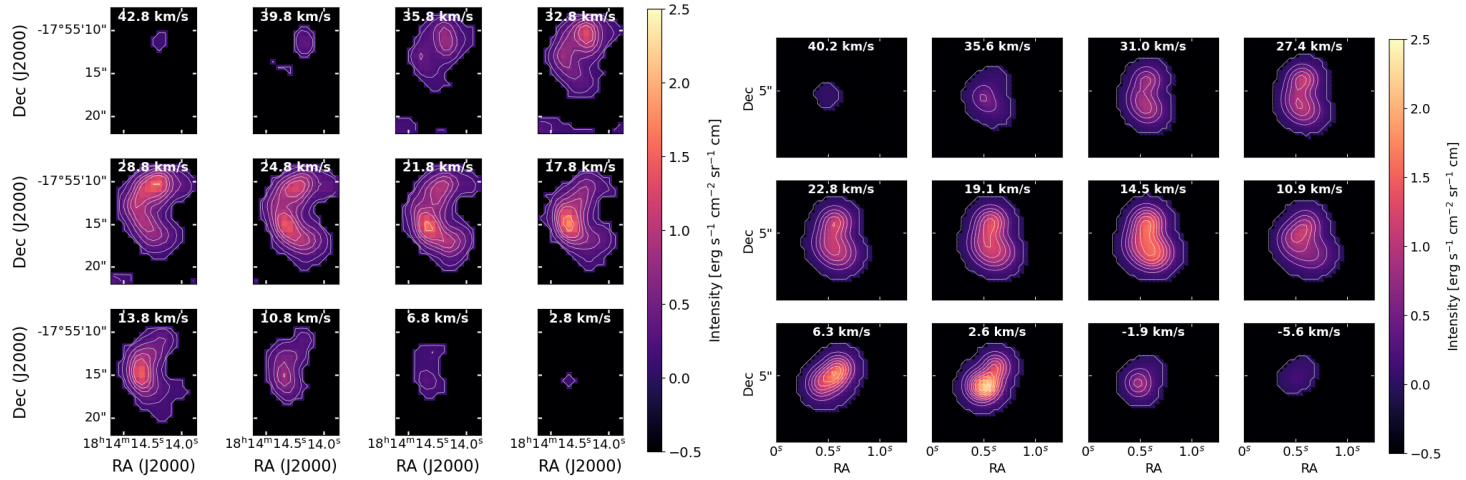
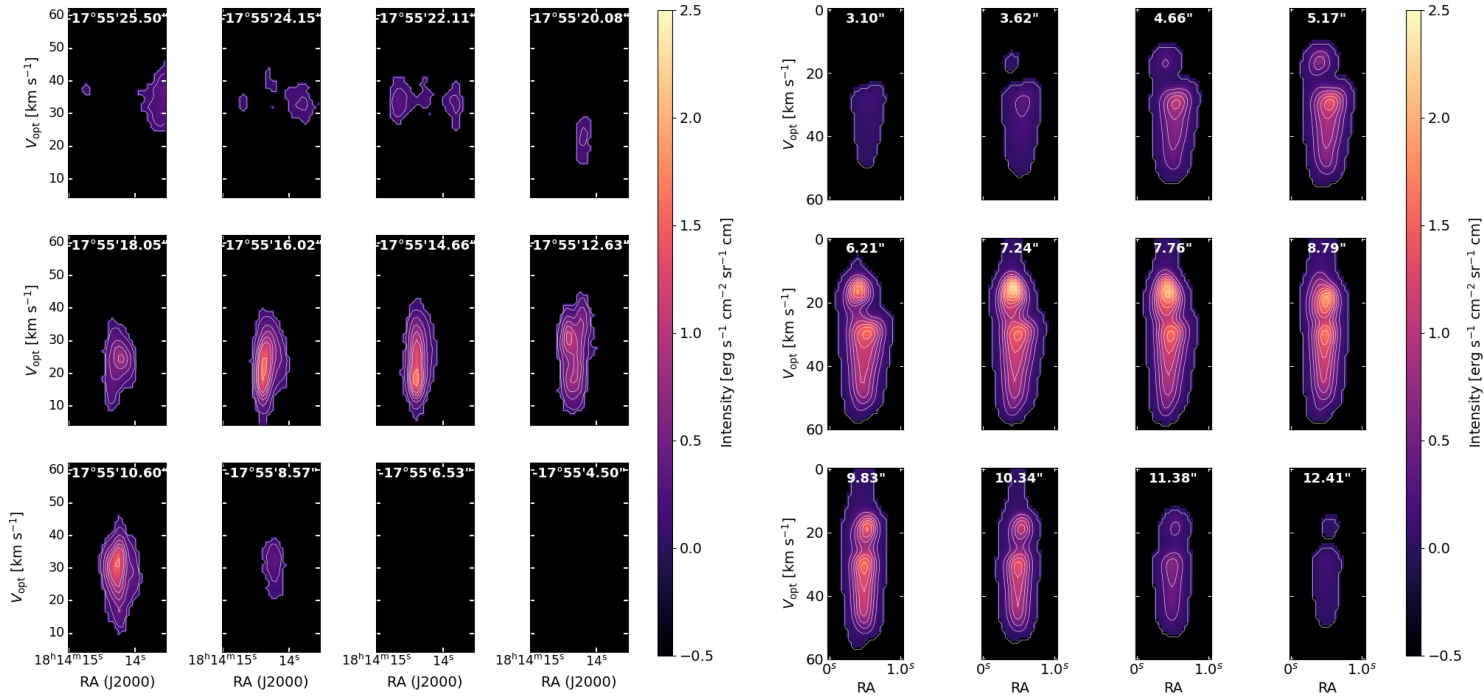


Figure 9. 3D View of the original [NeII] data cube cropped to the volume containing W33 Main 4 with the colored star movement curves (legend on bottom right) from 3 axes directions (Z- is the observer direction): (a) Dec, (b) RA, (c) Spectral/Kinematic. The X,Y,Z units are as follows: X axis is RA (1 X Unit = 0.66 arcsec), Y axis is Dec (1 Y Unit = 0.05s) and Z axis is spectral/kinematic axis (1 Z Unit = 1 km s^{-1}). The velocity axis is also denoted by the colored arrows where only the absolute velocity is considered. Each star curve shows the movement of a single star starting from the sphere shape and ending with the cube shape.



(a)

(b)



(c)

(d)

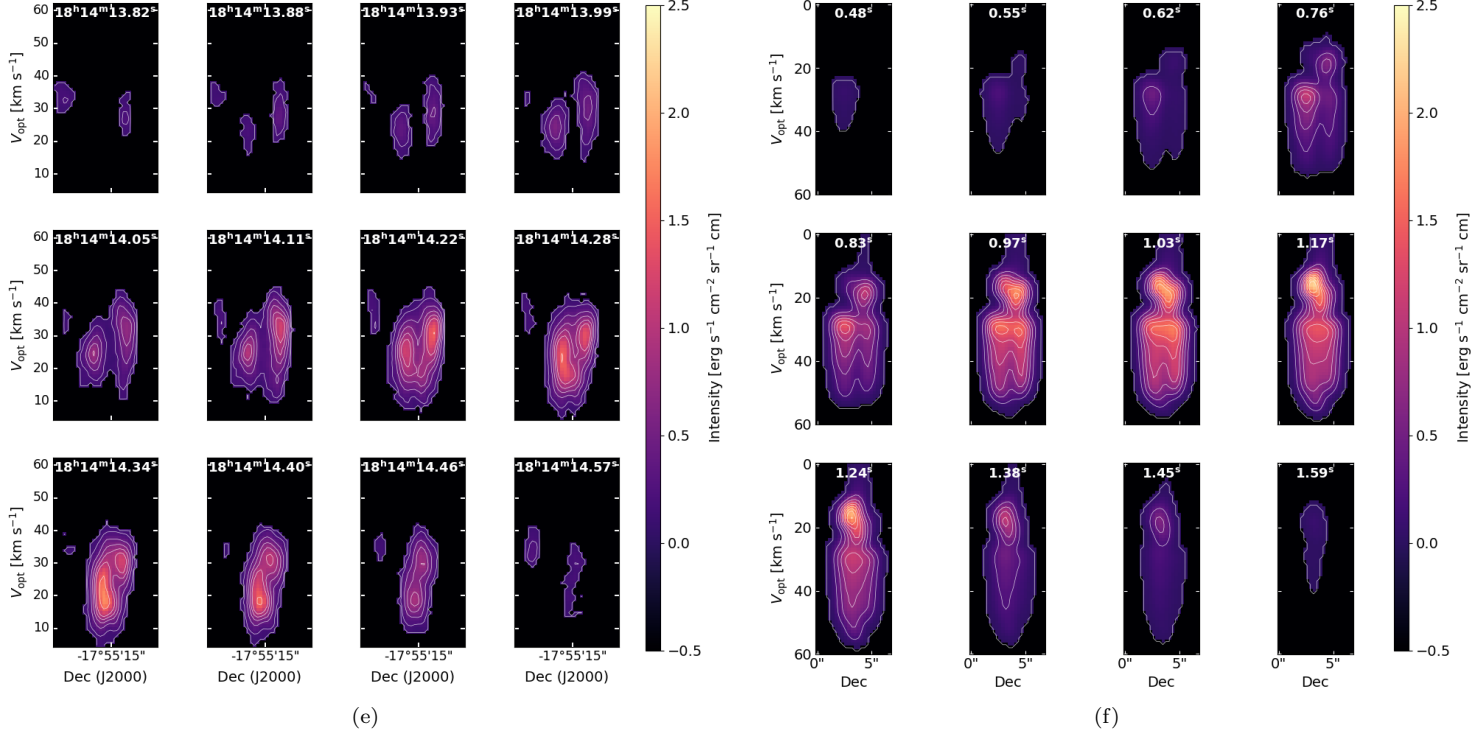


Figure 10. Comparison of the original data cube and the simulation results for W33 Main 4. Channel maps of (a) the [NeII] data cube cropped with contour levels at $[0.05, 0.1, 0.2, 0.5, 1.0, 1.5, 2, 2.5, 3]$ $\text{erg s}^{-1} \text{cm}^{-2} \text{sr}^{-1} \text{cm}$ and (B) line profile emission simulation results with contour levels at $[0.0, 0.5, 1, 1.5, 2, 2.5, 3.0, 3.3, 3.5, 3.7, 4.0]$ $\text{erg s}^{-1} \text{cm}^{-2} \text{sr}^{-1} \text{cm}$. Position-Velocity Diagrams in RA from the data cube (c) and the simulations (d). Position-Velocity Diagrams in Dec from the data cube (e) and the simulations (f).

Table 2. Predicted and Simulated Stellar Populations

UCHII Region	R_{region} [pc]	$M_{\text{region}}^{\text{min}}$ [M_{\odot}]	$N_{\text{predicted}}$	$N_{\text{simulation}}$
W33 Main 1 _a	0.13	60	4-5	7
W33 Main 1 _b	0.04	12	1	1
W33 Main 2 _a	0.11	49	3-4	5
W33 Main 2 _b	0.05	16	1	1
W33 Main 3 _a	0.05	18	1	1
W33 Main 3 _b	0.03	9	1	1
W33 Main 4	0.07	25	2	2

NOTE— Comparison of the predicted and simulated number of stars in each of W33 Main’s UCHII regions, with $N_{\text{predicted}}$ from the M_{region} of [Kauffmann et al. \(2010\)](#) and $N_{\text{simulation}}$ from our models.

- Each UCHII region can be simulated by a range of lower mass OB stars, moving relative to each other; the stars, the winds and their interactions interweave to create the complex kinematic and spatial structures seen in the data.
- The total stellar population suggested by the simulations is dominated by the lower-mass stars.

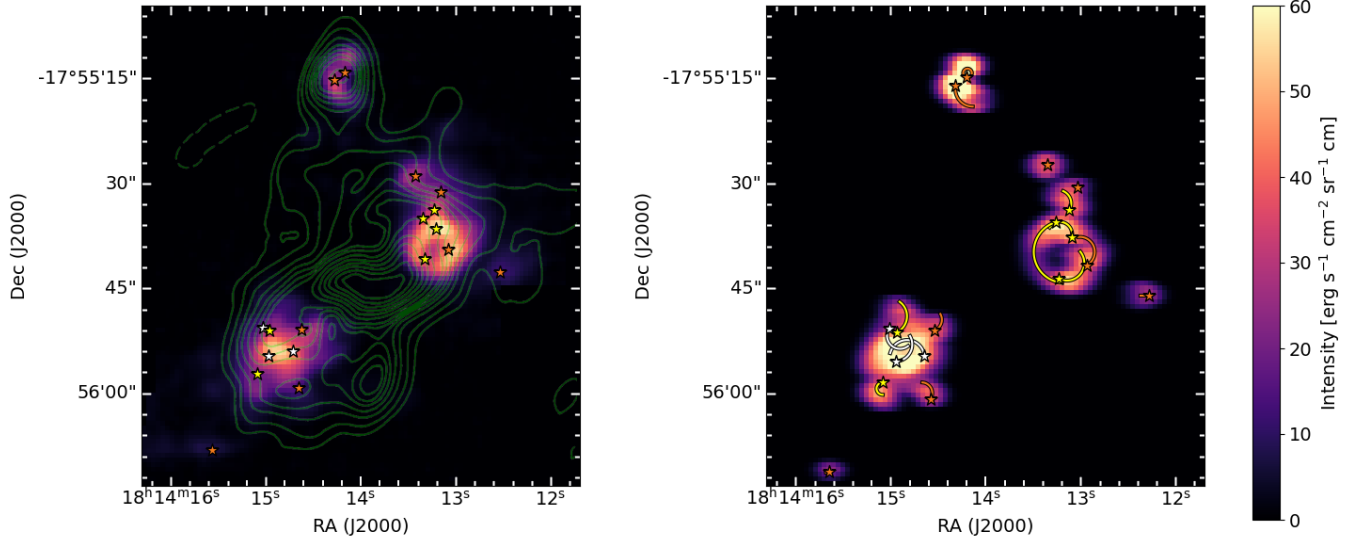


Figure 11. Comparison of the 0th moment map of the original W33 Main [NeII] data cube with the contours of the 6cm VLA radio map of W33 Main taken from [Haschick & Ho \(1983\)](#) (a) and the composite data cube (b) made up of all UCHII regions which we’ve simulated. On both maps the final position of each star in the simulations is denoted by colored star symbols, where their color indicates their mass (B0.5 - white, B1V - yellow, B1.5V - orange). The simulated composite map also shows their approximate movement during the simulations.

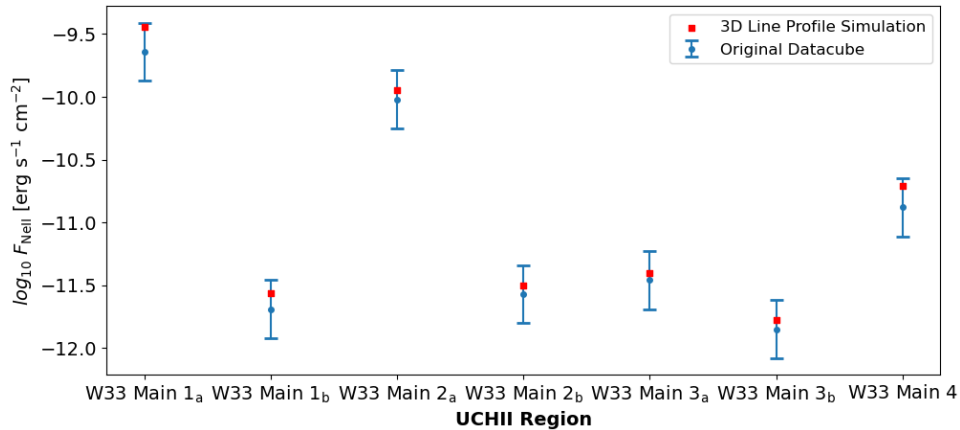


Figure 12. Comparison of total [NeII] flux of each UCHII region in W33 Main between the original data cube (blue circles) and the 3D line profile simulation results (red squares).

- The total ionization of the suggested stellar population slightly exceeds the observed [NeII] result, suggesting that some of the proposed ‘stars’ are density clumps or low mass stars, rather than ionizing OB stars. The worse discrepancy is in the complex source W33M1 and we think it possible that some of the ‘stars’ in the outer regions of that source are in fact non-ionizing. It may be that the central stars and gas are interacting to produce gas arms rather than the usual cometary shape on which the simulations are based ([Wang & Willson 2012](#)) or ([Homan et al. 2015](#))).

We have shown that models with multiple moving stars produce complex spatial and kinematic features, and have created such models consistent with the observations of W33 Main. But as in any simulation study, ‘consistent with the

observations' does not necessarily mean that the model is correct. A given spatial and velocity feature may have been created by any of several mechanisms. W33M2_a is a cautionary example. We have presented here models in which the many density features in W33M2_a (Figure 7) reflect structures in the ambient cloud or the wind. We interpreted these complicated internal structures as the 'curved tails' created by multiple stars in orbit, and the simulations show that this morphology can be created by a system of 4 stars. However the channel maps and PVDs of W33M2_a also resemble the cometary models of Zhu et al. (2015) in which there is a single stationary ionizing star and the two 'arms' of the PVD show gas flowing out of the UCHII region along the walls of a cavity. In those cometary models the ionized gas is predicted to be blue-shifted with respect to the embedding cloud; note that W33M2_a is $\sim 10 \text{ km s}^{-1}$ blue of the the molecular cloud velocity and of the other UCHII regions. Further observations with high resolution could determine which model, or combination of models, is most appropriate for this source.

Our results have suggested that the appearance and kinematics of UCHII regions may be created by interactions of multiple late-type OB stars. This picture can readily be checked with sub-arcsecond resolution radio mapping. If confirmed it will give a more accurate stellar population for the star formation region and a clue to the initial mass function. Another intriguing result of these simulations is that they point to the relative motions of the stars in each UCHII region. If confirmed, this model can show how the stellar proto-cluster W33 Main will develop, the trajectories of the stars and how the stars will disperse.

Finally, these results show the value not only of the simulations but of the data cube: the results depend on the very high spectral resolution possible with infrared lines of metal ions. The [NeII] data cube in W33 Main shows that the ionized gas has full velocity extent of only $\sim 40 \text{ km s}^{-1}$ and holds important kinematic features offset from each other by $\lesssim 10 \text{ km s}^{-1}$; it could not be studied properly under the $\sim 20 \text{ km s}^{-1}$ thermal broadening inevitable for an H I recombination line. This demonstrates the value of the metal ionic lines and of high spectral resolution in UCHII regions.

Facilities: JHL was a Visiting Astronomer at the Infrared Telescope Facility, which is operated by the University of Hawaii under contract 80HQTR19D0030 with the National Aeronautics and Space Administration.

7. APPENDIX

The 3D visualization program is available at https://github.com/danbeilis/fits_stellar_movement_viz. It offers an alternative method of analyzing the structure of data cubes by showing the structure in 3D. It makes it easy to examine different regions by limiting the range of the data shown; either by cropping the axes or selecting the intensity range. The program also makes it possible to add 2D slices along each of the three axes for a clearer view of the density structure. The program has the option of using arrows colored according to velocity to display kinematics without using the velocity axis. The 3D display changes instantly on changing the input parameters, which makes it simple to trace the trajectories of the stars and how they impact the UCHII regions.

8. DATA AVAILABILITY

The [NeII] data cubes are available in FITS format at <https://github.com/danbeilis/data/tree/master/W33>.

REFERENCES

- Beck, S., Kelly, D. M., & Lacy, J. 1998, AJ, 115, 2504
 Beck, S., Turner, J., Lacy, J., & Greathouse, T. 2015, ApJ, 814, 16
 Beck, S. C., Lacy, J., Turner, J., et al. 2020, MNRAS, 497, 1675
 Churchwell, E. 2002, ARA&A, 40, 27
 Churchwell, E., Babler, B. L., Meade, M. R., et al. 2009, PASP, 121, 213
 Courant, R., Friedrichs, K., & Lewy, H. 1967, IBM J. Res. Dev., 11, 215
 Dullemond, C., Juhasz, A., Pohl, A., et al. 2012, ASCL, ascl
 Dyck, H., & Simon, T. 1977, ApJ, 211, 421
 Gardner, F., Wilson, T., & Thomasson, P. 1975, ApJ, 16, 29
 Genzel, R., & Downes, D. 1977, A&AS, 30, 145
 Harten, A., Lax, P. D., & Leer, B. v. 1983, SIAM Rev., 25, 35
 Haschick, A., & Ho, P. 1983, ApJ, 267, 638
 Haschick, A. D., Menten, K. M., & Baan, W. A. 1990, ApJ, 354, 556
 Homan, W., Decin, L., de Koter, A., et al. 2015, A&A, 579, A118
 Immer, K., Galván-Madrid, R., König, C., Liu, H., & Menten, K. 2014, A&A, 572, A63

- Immer, K., Reid, M., Menten, K., Brunthaler, A., & Dame, T. 2013, *A&A*, 553, A117
- Jaffe, D., Zhu, Q., Lacy, J., & Richter, M. 2003, *ApJ*, 596, 1053
- Kauffmann, J., Pillai, T., Shetty, R., Myers, P. C., & Goodman, A. A. 2010, *ApJ*, 712, 1137
- Kohno, M., Torii, K., Tachihara, K., et al. 2018, *PASJ*, 70, S50
- Krtićka, J. 2014, *A&A*, 564, A70
- Kurtz, S., Churchwell, E., & Wood, D. 1994, *ApJS*, 91, 659
- Lacy, J., Beck, S., & Geballe, T. 1982, *ApJ*, 255, 510
- Lacy, J., Richter, M., Greathouse, T., Jaffe, D., & Zhu, Q. 2002, *PASP*, 114, 153
- Lamers, H. J., & Leitherer, C. 1993, *ApJ*, 412, 771
- Mac Low, M.-M., Van Buren, D., Wood, D. O., & Churchwell, E. 1991, *ApJ*, 369, 395
- Mackey, J., Gvaramadze, V. V., Mohamed, S., & Langer, N. 2015, *A&A*, 573, A10
- Martin, D. C., Seibert, M., Neill, J. D., et al. 2007, *Nature*, 448, 780
- Meyer, D.-A., Mackey, J., Langer, N., et al. 2014, *MNRAS*, 444, 2754
- Mignone, A. 2014, *J. Comput. Phys.*, 270, 784
- Mignone, A., Bodo, G., Massaglia, S., et al. 2007, *ApJS*, 170, 228
- Pittard, J., Wareing, C., & Kupilas, M. 2021, *Monthly Notices of the Royal Astronomical Society*, 508, 1768
- Van Buren, D., & Mac Low, M.-M. 1992, *ApJ*, 394, 534
- van der Helm, E., Saladino, M. I., Zwart, S. P., & Pols, O. 2019, *A&A*, 625, A85
- Walsh, A., Burton, M., Hyland, A., & Robinson, G. 1998, *MNRAS*, 301, 640
- Wang, Q., & Willson, L. A. 2012, *ApJ*, 755, 136
- Weaver, R., McCray, R., Castor, J., Shapiro, P., & Moore, R. 1977, *ApJ*, 218, 377
- Wilkin, F. P. 1996, *ApJ*, 459, L31
- Wood, D. O., & Churchwell, E. 1989a, *ApJS*, 69, 831
- Zhu, F.-Y., Zhu, Q.-F., Li, J., Zhang, J.-S., & Wang, J.-Z. 2015, *ApJ*, 812, 87
- Zhu, Q.-F., Lacy, J. H., Jaffe, D. T., Richter, M. J., & Greathouse, T. K. 2008, *ApJS*, 177, 584